JOURNAL OF GEOPHYSICAL RESEARCH, VOL. 103, NO. C6, PAGES 12,613–12,628, JUNE 15, 1998

Coupling of internal waves on the main thermocline to the diurnal surface layer and sea surface temperature during the Tropical Ocean–Global Atmosphere Coupled Ocean-Atmosphere Response Experiment

E. J. Walsh,[1,2] R. Pinkel,[3] D. E. Hagan,[4] R. A. Weller,[5] C. W. Fairall,[6] D. P. Rogers,[3] S. P. Burns,[7] and M. Baumgartner[7]

Abstract. Patterns in sea surface temperature (SST) on 5-km scales were observed from low-flying research aircraft on a light wind day during the Tropical Ocean–Global Atmosphere Coupled Ocean-Atmosphere Response Experiment. An inverse trend was observed between the SST and the sea surface mean square slope (mss). However, low correlation coefficients indicate that the dominant process causing the spatial variation of SST under these light wind conditions is neither well controlled by the wind speed nor well monitored by the mss. The SST spatial pattern persisted for at least 1 hour and propagated toward the NE at about 1 m s^{-1}, a factor of 1.6 faster than the speed of the surface current. Coupling between internal gravity waves propagating on the seasonal thermocline and the diurnal surface layer is examined as a possible explanation for the observed SST variability in space and time.

1. Introduction

This paper deals with data collected on November 28, 1992, during the Tropical Ocean–Global Atmosphere (TOGA) Coupled Ocean-Atmosphere Response Experiment (COARE) in the western equatorial Pacific "warm pool" [*Webster and Lukas*, 1992]. On that day and during other periods of light winds it was observed that spatial patterns in sea surface temperature (SST) on scales of several kilometers to 100 km persisted and were observed on successive aircraft overflights which were as much as 2 hours apart [*Hagan et al.*, 1997]. The anomaly amplitudes in the SST associated with these patterns were of the order of 0.5°C.

SST variability results largely from the contributions of the fluxes at and near the sea surface and entrainment of cooler water across the mixed layer base, as was demonstrated by *Price et al.* [1986]. Spatial patterns in heat flux and rain can imprint themselves on the sea surface. The wind-driven velocity in the mixed layer is proportional to the wind stress and inversely proportional to the depth of the layer. As a result, increased shear and mixing across the base could result from either higher wind stress or a reduction in layer thickness, and spatial structure in both the wind and the mixed layer depth can also produce spatial patterns in SST.

The light westerly wind on November 28 does not appear to be the origin of the observed spatial variation in SST. Nor does spatial variability in the surface heat and freshwater fluxes. Instead, we believe the observed patterns to reflect the presence of internal waves.

On November 28 a WP-3D aircraft of the National Oceanic and Atmospheric Administration (NOAA) flew in formation with the National Center for Atmospheric Research (NCAR) Electra aircraft on a six-leg track over the Woods Hole Oceanographic Institution (WHOI) IMET buoy (Figure 1). The Obukhov length scale, $-L$, was approximately 7 m for this day [*Serra et al.*, 1997]. Since $-L$ is a measure of the height at which buoyant production of turbulent kinetic energy exceeds shear production, the atmospheric boundary layer was under strong, free convection. Midlatitude values of $-L$ typically exceed 300 m. The wind stress measured at the IMET buoy was about 0.005 N m^{-2} toward 80°. The mean air temperature at 10 m was 29.07°C, and the air-sea temperature difference averaged about -1.6°C. The mean specific humidity was 17.89 g kg^{-1}.

There were dominant, persistent spatial SST patterns whose translation speed (0.8–1.2 m s^{-1}) was too fast to be explained as advection by the surface current (0.4–0.7 m s^{-1}) and too slow to be explained by the wind speed (2 m s^{-1}, 1.6 m s^{-1} relative to the surface current). Thus we were led to investigate the possibility that internal gravity waves [*Ewing*, 1950] propagating in the ocean along the main thermocline were the cause of the observed spatial structure in SST.

Section 2 discusses the semidiurnal tide internal wave in evidence in the IMET mooring measurements which caused the principal spatial variation of the near-surface current. Section 3 discusses the measurement of SST from an aircraft and compares the radiometer observations with in situ measurements. Section 4 examines the correlations of SST with wind speed and sea surface mean square slope (mss) and eliminates

[1]Observational Science Branch, Laboratory for Hydrospheric Processes, NASA Goddard Space Flight Center, Wallops Island, Virginia.
[2]On assignment at NOAA Environmental Technology Laboratory, Boulder, Colorado.
[3]Scripps Institution of Oceanography, La Jolla, California.
[4]Jet Propulsion Laboratory, Pasadena, California.
[5]Woods Hole Oceanographic Institution, Woods Hole, Massachusetts.
[6]NOAA Environmental Technology Laboratory, Boulder, Colorado.
[7]Department of Mechanical Engineering, University of California, Irvine.

Paper number 98JC00894.
0148-0227/98/98JC-00894$09.00

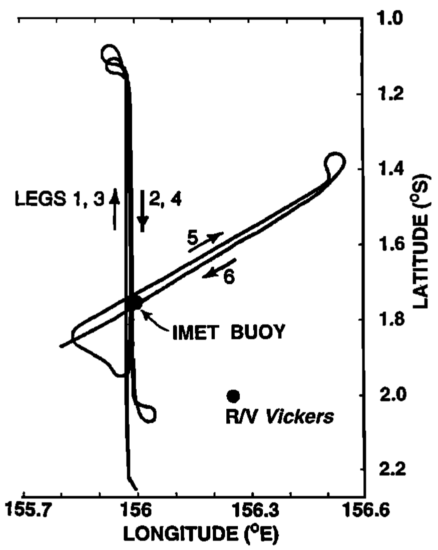

Figure 1. NOAA WP-3D ground track on November 28, 1992. The locations of the WHOI IMET buoy (1.75°S, 156°W) and R/V *Vickers* (2°S, 156.25°E) are indicated by the filled circles.

wind speed variation as a possible explanation of the observed spatial patterns of SST.

Section 5 discusses the remarkable characteristics of the SST spatial patterns observed by the aircraft and eliminates advection by the current as a possible explanation for their translation. Section 6 discusses the modulation of the diurnal surface layer by internal waves with periods shorter than the semidiurnal tide. Section 7 discusses other experiments which suggest that internal waves modulate SST and demonstrates that the translation speed of the SST spatial pattern is in the range of phase speeds for mode 2 internal waves of the appropriate wavelength range. All times cited in this paper are in coordinated universal time unless specified otherwise.

2. IMET Mooring Measurements

The Woods Hole Oceanographic Institution (WHOI) 3-m discus buoy [*Weller and Anderson*, 1996] mooring (1.75°S, 156°E) was named IMET for its improved meteorological package, but it also measured water properties at a variety of depths. IMET measured water temperature every 15 min using Brancker temperature recorders (TPOD) at six depths in a near-surface array between 0.45 and 2.5 m and also at ten depths between 27 and 260 m. Measurements were recorded every 3.75 min with 14 SeaBird conductivity and temperature (SEACAT) sensors between 2 and 108 m. SEACATs at 84- and 124-m depth were sampled at 5-min intervals. Except for the SEACAT at 2-m depth, there was only 15-min sampling at depths above 5 m or below 124 m.

Figure 2 shows three temperature profiles made on November 28, 1992. The diurnal surface layer, confined to the top few meters, will be discussed later. The mixed layer extended down to about 50-m depth. Below the mixed layer the temperature decreased approximately linearly through the thermocline, whose bottom was at about 200- to 250-m depth.

Internal gravity waves can propagate through stably stratified fluids. They are ubiquitous in the main thermocline of the world's oceans [*Garrett and Munk*, 1979]. The equatorial Pacific is a particularly energetic region. Time series of current and temperature made during TOGA COARE indicate that large-amplitude (20 m) tidally forced internal waves propagating toward the northeast are common, apparently generated by topography to the southwest [*Pinkel et al.*, 1997]. The profiles in Figure 2 indicate that the thermocline was significantly higher at 0655 than it was either 6 hours earlier (0055) or 6 hours later (1255). This vertical motion resulted from the propagation of a semidiurnal tidal internal wave of about 3 m s^{-1} phase speed and 130-km wavelength. The phase speed was determined from observations of the Väisälä frequency at R/V *Vickers* (2°S, 156.25°E) between 0700 and 1000 on November 28, 1992. The wavelength follows from the semidiurnal period.

The top panel of Figure 3 shows a schematic representation of the displacement of the thermocline as an internal wave propagates and indicates the currents induced near the sea surface. Sufficiently nonlinear internal waves can take on a trochoidal appearance. When the water depth below the thermocline (about 2000 m in the region shown in Figure 1) is greater than the water height above it, the crests of the internal wave are broad and the troughs are sharp, as is indicated in Figure 3 [*LaFond and Cox*, 1962; *Apel et al.*, 1985]. Downwelling regions occur following the passage of wave crests; upwelling regions precede their arrival. These are the sites of maximal sea surface convergence and divergence, respectively. The maximum of the time integral of the convergence is over the trough, and the maximum integrated updraft is over the crest.

The second panel of Figure 3 shows five isotherms for a 36-hour period surrounding the aircraft flight. The time axis in Figure 3 has been reversed to increase from right to left so the IMET temporal observations will correspond to the spatial schematic representation in the top panel. Reversing the time axis implicitly incorporates the time to space conversion for a spatial structure propagating from left to right past a fixed observation point.

The semidiurnal period dominates the isotherms, although

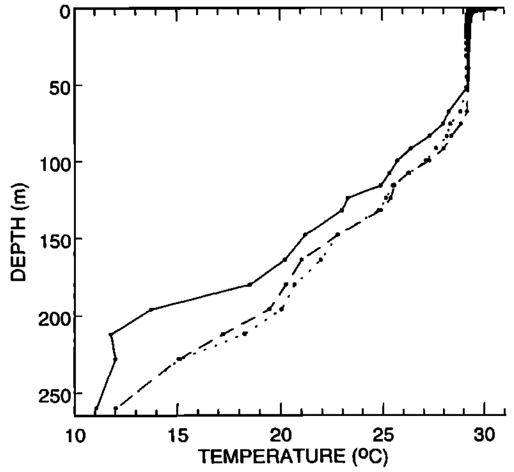

Figure 2. IMET temperature profiles made at 0055 (dotted), 0655 (solid), and 1255 (dashed) UTC on November 28, 1992. Brancker temperature recorders (TPOD), sampled at 15-min intervals, were at depths of 0.45, 0.55, 1.1, 1.6, 2.65, 4.65, 27, 35, 132, 164, 180, 196, 212, 228, 244, and 260 m. SeaBird conductivity and temperature (SEACAT) sensors, sampled every 3.75 min, were at depths of 2, 7.5, 11.5, 15.5, 19.5, 23.5, 31.5, 39.5, 45.5, 52.5, 76, 92, 100, and 108 m. SEACATs at 84- and 124-m depth were sampled at 5-min intervals.

higher-frequency variations are also apparent. The vertical displacements associated with internal waves diminish above the thermocline, and there is almost no displacement signature at the surface. However, the induced currents persist to the surface.

The IMET mooring measured current vectors at 24 depths, from 5 to 325 m. The two lower panels of Figure 3 show the total and the low-frequency (15.3-hour period or greater) component of the current speed and direction measured at 5-m depth by a vector measuring current meter (VMCM) sampled at 3.75-min intervals. The current data in Figure 3 are plotted at the 15-min resolution of the isotherms. It is apparent that a semidiurnal period dominates the high-frequency component of the current.

The current speed had local maxima in the vicinity of the internal wave troughs at about 0000 and 1200, indicating that the semidiurnal component was roughly aligned with the mean current at those times. The current minimum occurred about midway between, when the semidiurnal component opposed the mean current. That suggests that the semidiurnal tide internal wave was propagating toward 60°, the direction of the mean current. The alignment with the mean current is coincidental, but this direction of propagation is typical of internal waves in this region [*Pinkel et al.*, 1997].

We will later have need of the current variation along leg 5 and will now obtain it through a spatial projection from the temporal measurements at the IMET mooring. The north and east components of the current observations at 5-m depth were separated into high- and low-frequency intervals, with the boundary being a period of 15.3 hours chosen on the basis of minimum spectral energy. The high-frequency current components were assumed to be induced by the internal wave that is the semidiurnal tide in this region as it propagated by IMET. They were projected spatially toward 60°, using the 3 m s^{-1} phase speed. The low-frequency current components were assumed to exist simultaneously throughout the overflight region. The low-frequency north and east IMET components at each observation time were added to the high-frequency components projected from earlier or later IMET measurements depending on whether the observation point was NE or SW of the mooring.

Figure 4 shows the variation along leg 5 of the 60° component of the composite current (solid curves) for two different time intervals separated by about an hour. The components were nearly equal to the current itself since the current and the ground track were so closely aligned.

It should be noted that the low-high frequency decomposition and spatial projection of the current in no way underestimated its value. The current at IMET never exceeded 45 cm s^{-1} during our measurement interval (indicated by the three solid vertical lines in Figure 3), yet the maximum 60° current component in our projection exceeds the 70 cm s^{-1} peak value recorded by IMET 4 hours before we began taking data. This is because the low-frequency current component was increasing. It took about 5.5 hours for the semidiurnal tide peak current observed by IMET at 0000 to propagate to the east end of leg 5, where its amplitude was added to the larger low-frequency current component occurring at that later time.

3. Measurement of SST From Aircraft

The SST data presented in this paper were obtained from the Barnes PRT-5 radiometer on the NOAA WP-3D aircraft

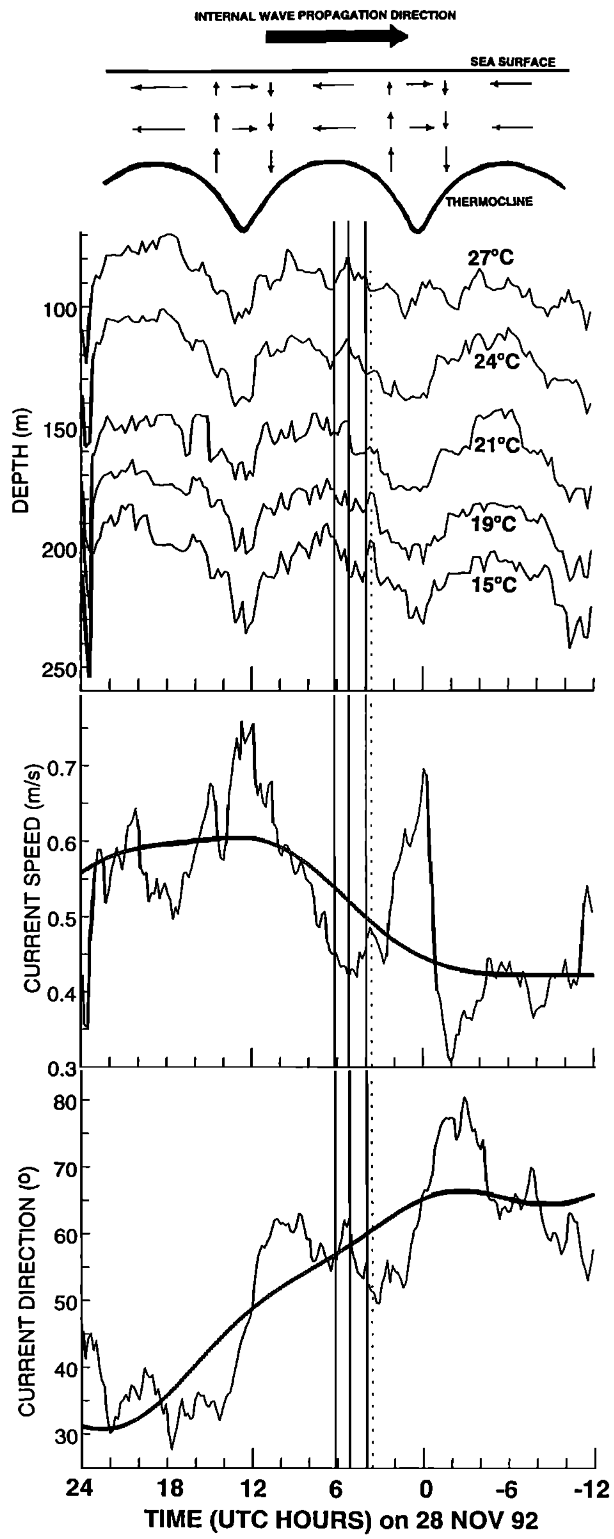

Figure 3. (top) Schematic representation of the deflection of the thermocline and the currents induced by a nonlinear internal wave in deep water and five isotherms from IMET data, with total (thin curve) and low-frequency component (thick curve) of (middle) IMET 5-m depth current speed and (bottom) direction. The three vertical solid lines indicate the starting time of leg 1 (Figure 1), the midpoint of leg 5, and the midpoint of leg 8 (nearly a reverse transit of leg 5). Time increases from right to left to implicitly incorporate the time to space conversion for a spatial structure propagating from left to right past an observation point.

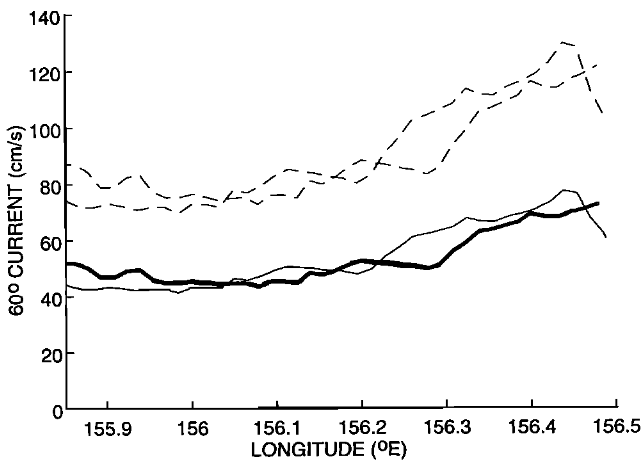

Figure 4. Spatially extrapolated values for the current component parallel to the ground track which were used to shift the SST transects. The thin solid curve is the extrapolated current component for leg 5 (northeast transect) and the thick solid curve is for leg 8 (southwest transect). The dashed curves are the solid curves multiplied by a factor of 1.68.

N43RF and from the NASA Jet Propulsion Laboratory (JPL) SST radiometer on the NCAR Electra aircraft 308D. The PRT-5 radiometer was located toward the tail section of the NOAA aircraft and viewed the ocean through a small nadir port. It has a 2° field of view (FOV) and operates in the thermal IR region between 8 and 12 μm. This spectral region, often called the atmospheric "window" region, is commonly used for measurements of sea surface brightness temperature. The PRT-5 was calibrated before and after deployment to the Solomon Islands. For the range of temperatures reported here the pre-mission and post-mission calibration curves agreed to within 0.15°C, well within the nominal accuracy of the instrument (0.5°C).

The JPL SST radiometer on the NCAR aircraft has a 1-mrad FOV and a collecting aperture of 20 cm. The radiometer telescope was configured with an optical filter in the 10- to 11-μm region. The instrument has a laboratory calibration accuracy of 0.1°C and a precision of 0.002°C at 20°C (at 293 K and 0.1 Hz). The radiometer was mounted in the forward baggage compartment of the Electra and viewed the ocean through a germanium window. The window temperature was monitored to correct the detected radiance for the contribution by the window emission [*Hagan et al.*, 1997].

Measurements from the two radiometers agreed to within about 0.2°C, when obtained wingtip to wingtip at the same altitude. To compare the radiometric data sets with each other and with the ocean in situ measurements, the data were corrected for atmospheric attenuation and sea surface emissivity effects. Sky emission was measured by an upward looking PRT-5 radiometer on board the Electra. These measurements were used to correct the JPL measurements for effects of nonblackness in the sea surface emissivity. The emissivity adjustment determined from the Electra measurements (+0.3°C) was applied to the NOAA downward looking PRT-5 observations, since sky radiation measurements were not available on the WP-3D. The signal attenuation due to absorption path length between the aircraft and surface was determined empirically as 0.08°C per 30 m, in reasonable agreement with estimates derived from radiative transfer calculations using a standard tropical atmosphere model.

Under some circumstances, specular reflections of the Sun in the FOV of a radiometer can contaminate its measurements. The analysis in the appendix of *Saunders* [1967] indicates that the biggest effect for a nadir directed radiometer under light winds occurs for a solar elevation angle of 90°. The largest solar elevation angle during the present data acquisition was 55°. Since the aircraft attitude caused the radiometers to deviate from nadir by only 1°–2° during the flight lines, *Saunders* [1967] indicates that solar specular reflections were entirely negligible.

Figure 5 shows a region near the IMET mooring, with segments of the six ground tracks shown in Figure 1 and two additional ground tracks flown after the NCAR Electra aircraft had departed the area. The R/V *Moana Wave* measured fluxes and water properties about 4 km north of IMET during this period. Its positions during the legs are also indicated.

Figure 6 shows SST measurements for 12-km-long segments from each leg, centered on the point of closest approach to IMET. No smoothing was applied to these 1-s data. At zero along-track distance, the circle is the IMET SST determined from the TOGA COARE bulk algorithm [*Fairall et al.*, 1996b], which includes both the diurnal surface layer and the cool skin effects; the cross is the IMET sea temperature at 0.45-m depth. At the minimum of the dotted curve, the plus symbol is the sea temperature measured at about 5-cm depth at the R/V *Moana Wave*; the circle at the same position is the SST estimate arrived at by subtracting the cool skin temperature difference computed from the TOGA COARE bulk algorithm from the 5-cm-depth temperature measurement. The *Moana Wave* and IMET SST estimates are generally in good agreement with the aircraft measurements considering the ground track locations and the spatial gradients.

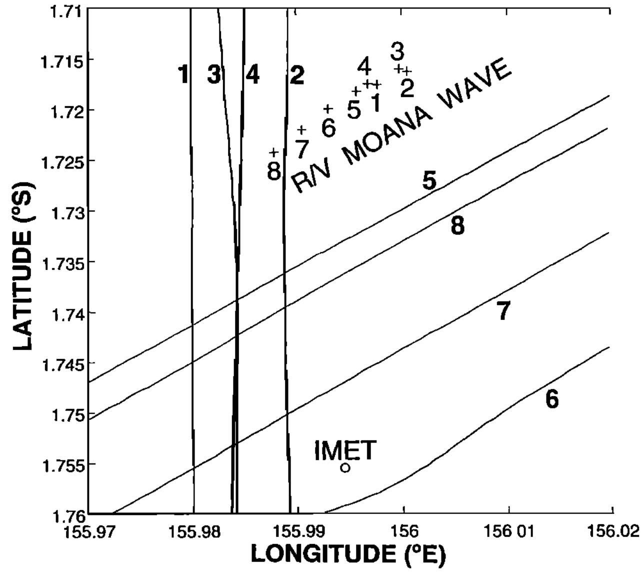

Figure 5. Segments (bold numbers) of the six ground tracks shown in Figure 1 and two additional ground tracks flown after the NCAR Electra aircraft left the area. The plus symbols indicate the positions (regular numbers) of R/V *Moana Wave* during each numbered leg. The IMET mooring position is indicated by the circle.

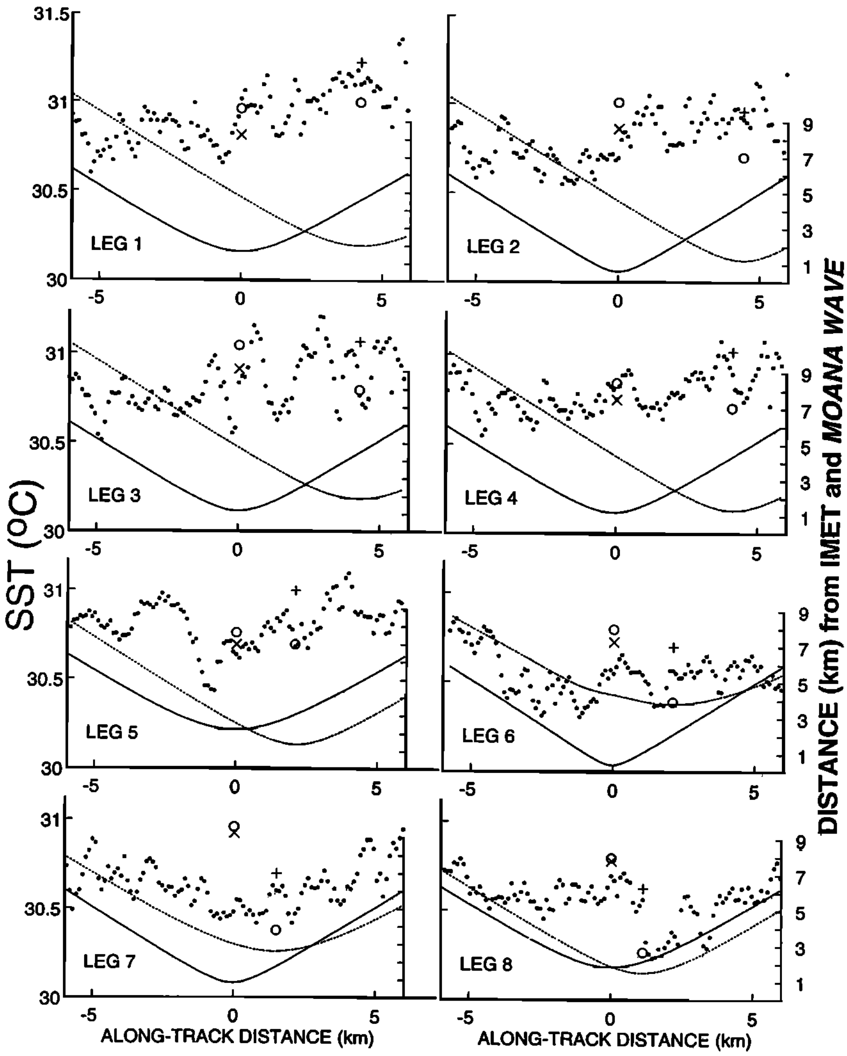

Figure 6. SST measurements for 12-km-long segments from each leg, centered on the point of closest approach to the IMET mooring. No smoothing was applied to these 1-s data. The abscissa is negative for positions southwest of the point of closest approach to IMET and positive for positions northeast, independent of the flight direction. The curves indicate the distance of each measurement from IMET (solid) and from the R/V *Moana Wave* (dotted). The symbols are described in section 3 of the text.

4. SST Variation With Wind Speed and Mean Square Slope

Figure 7 shows data from leg 1 of Figure 1. The general variation of the SST appears to be inversely correlated with mss over the leg, with SST resembling a W and mss resembling an M. The same is true to a lesser extent with SST and wind speed. At 2.04°S there is a 1 m s^{-1} local minimum in wind speed that corresponds to a local minimum in mss and a maximum in SST. In general, however, the variations in mss, wind speed, and SST on spatial scales of a few kilometers do not correlate well.

The SST dependence on wind speed alone is indicated in Figure 8. The circles indicate the nominal variation with wind speed of the peak afternoon temperature of the diurnal surface layer determined from the *Fairall et al.* [1996a] warm layer model, while the stars show the wind speed dependence observed by *Soloviev and Lukas* [1997] during COARE. The power laws fitted to Figure 8 also appear in Figure 9, which shows the SST data from flight lines 1–6 versus wind speed relative to the surface. Both the SST and the wind speed are accurate (see *Walsh et al.* [this issue] (hereinafter referred to as paper 2) for details of the wind speed measurement), but the high-low-high-low variation of the correlation coefficients on the first four legs, where there are relatively small temporal and spatial changes because the aircraft just keeps reversing heading, emphasizes the tenuous nature of the relationship.

The transient response to a fluctuating wind speed would be expected to be less than is indicated in Figure 8, since it takes time to redistribute the near-surface heat over a greater depth. However, the weak dependence of SST on wind speed also suggests processes other than just the interplay of surface forcing and entrainment encapsulated by the *Price et al.* [1986] mixed layer dynamics built into the COARE algorithm. This notion is reinforced by the larger negative correlation found between mss and SST as seen in Figure 7 but also seen more generally over all six legs in Figure 10.

Wind speed and mss are positively correlated [paper 2], but internal waves can also give rise to patterns in mss. The convergent currents they generate have been described as accumulating over the trough of the internal wave both warm sur-

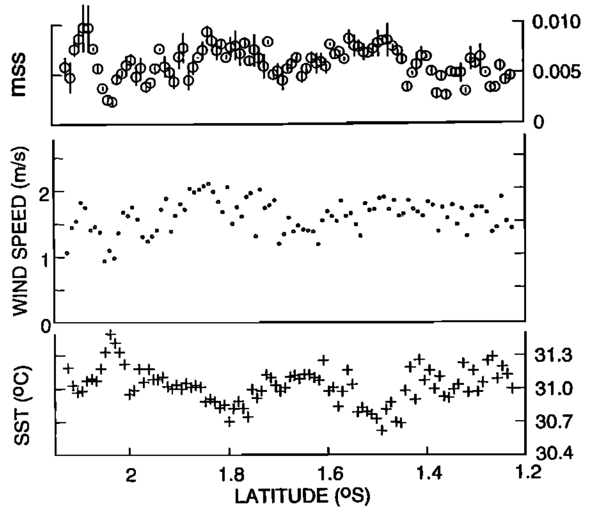

Figure 7. Mean square slope, wind speed relative to the surface, and SST versus latitude for leg 1. The vertical lines through the mss circles indicate the 1σ error bars on the mean values.

face water and surfactants, which would tend to decrease mss [*LaFond and Cox*, 1962; *Fedorov and Ginsburg*, 1988; *Kropfli et al.*, 1998]. *Etkin et al.* [1992] reported that slick regions measured off Kamchatka under light wind conditions during the day had surface temperatures measured with an IR radiometer that were 1.5°–2°C higher than those of rough regions.

5. Spatial Variation of SST

On legs 1 and 5 of Figure 1, NOAA WP-3D aircraft N43RF flew wingtip to wingtip with NCAR Electra aircraft 308D at 60-m height with about 100-m separation between their fuselages. The top panel of Figure 11 shows an overlay of the simultaneous SST measurements on leg 1 from the PRT-5 radiometer on the NOAA WP-3D N43RF (solid curve) and the JPL radiometer on the NCAR Electra 308D (dots). The bottom panel of Figure 11 is a similar overlay, but from leg 5. A constant bias of 0.2°C has been added to the JPL radiometer data from leg 5 for this comparison. The latitudes and longitudes indicated in this paper are from the N43RF GPS-corrected Inertial Navigation Equipment (INE) data (see appendix).

The relative SST variations in both panels of Figure 11 are in excellent agreement. These 1 Hz data were time shifted with respect to each other to determine the alignment with the highest correlation. The 0.98 correlation for the 60° flight direction (Figure 11, bottom) was obtained with no time shift, indicating that the long axis of these features was oriented perpendicular to that ground track. The 0.96 maximum correlation for the north flight direction (top) was obtained when the NCAR Electra data were shifted 1 s earlier in time. The aircraft ground speed on that leg was 111 m s^{-1}, and the NCAR Electra was about 100 m to the right of the NOAA P-3. This suggests that the long axis of the features was oriented perpendicular to 48°, quite consistent with the 60° flight direction conclusion, considering the temporal quantization. The minor differences in the remarkable agreement of these independent temperature measurements could be attributed to the 100-m lateral displacement of the aircraft ground tracks.

The NCAR Electra departed the area soon after leg 6 was completed. An hour after the initial northeast transit (leg 5), N43RF made a nearly overlying southwest transit (leg 8, Figure 5). Figure 12 indicates the north-south deviations of legs 5 and 8 from a straight line passing through leg 5. The southwest transit maintained a nearly constant 400-m offset south of the northeast ground track along most of its length.

The top panel of Figure 13 shows SST from the N43RF PRT-5 radiometer on legs 5 and 8. The correlation coefficient for the SST measurements on leg 5 (solid curve, identical to the solid curve in the bottom panel of Figure 11) and leg 8 (dots) was 0.73. Because similar structure was recognized in the two SST transects, an attempt was made to shift them into better alignment.

Legs 5 and 8 had orientations close to the mean current direction, and the direction of propagation of the semidiurnal tide internal wave. The first attempt was an ad hoc assumption that the SST structure was rigidly imbedded in the sea surface and advected by the current. A reference time was taken halfway between the end of leg 5 and the start of leg 8.

The overflights on November 28 occurred in the afternoon under diminishing solar heating. A linear regression to the SST

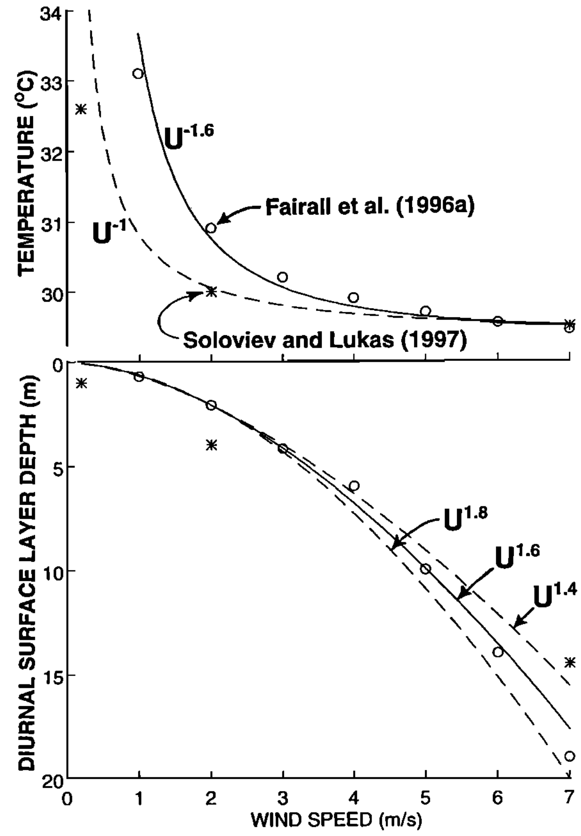

Figure 8. Expected variation with wind speed of (top) the peak afternoon temperature of the diurnal surface layer (not including the cool skin) and (bottom) the depth of the diurnal surface layer for the conditions of the November 28 flight, computed from the *Fairall et al.* [1996a] warm layer model (circles). Results using *Soloviev and Lukas* [1997] measurements are indicated by asterisks. The water at 5-m depth was within 0.16°C of 29.3°C from November 25 through November 28. The plotted temperatures were arrived at by adding the cited temperature differences across the diurnal surface layer to 29.3°C. Curves show several power law dependencies on wind speed for comparison.

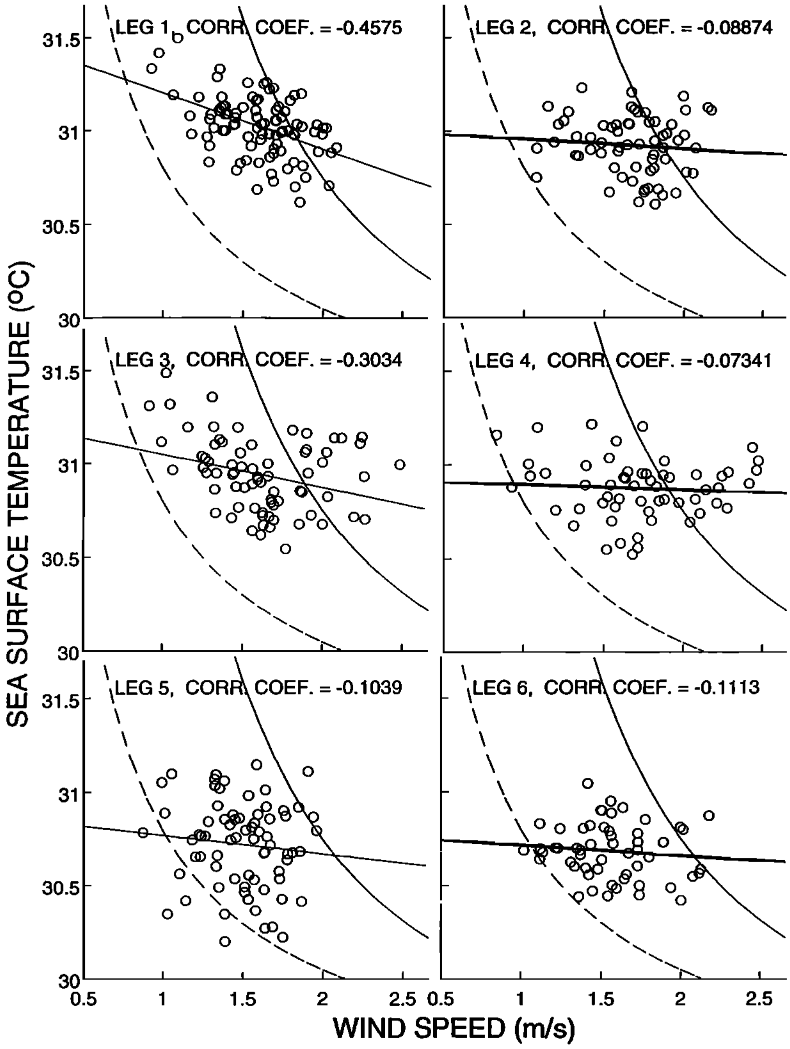

Figure 9. SST data points for each of flight lines 1–6 versus wind speed relative to the surface, with linear regression lines. The dashed and solid curves are the same as in the top panel of Figure 8.

data from flight lines 1–6 indicated SST cooling at a rate of 0.24°C h^{-1} [paper 2]. SST values were extrapolated from the two measured transects to the reference time assuming that all the SST values decreased at the 0.24°C h^{-1} rate. The positions along the ground track changed by an amount determined by the time interval between the measurement time and the reference time multiplied by the component of the current vector parallel to the ground track at the measurement point (solid curves in Figure 4). The result is shown in the middle panel of Figure 13. The agreement is considerably improved, and the correlation coefficient has increased to 0.81.

The second attempt to shift the SST patterns from the two flight legs into better agreement was done under the assumption that the patterns translated at speeds faster than the surface current but in the same direction. If the translation speeds are increased above the surface currents by a factor of 1.68 (dashed curves in Figure 4), the correlation coefficient increases to 0.91 (bottom panel of Figure 13). This is remarkable agreement considering not only the hour between the flight lines, but their 400 m lateral displacement. The aircraft separation for the simultaneous data of Figure 11 was only ~100 m.

If the NCAR Electra JPL radiometer curve (dotted curve in the bottom panel of Figure 11) were substituted for the solid curve in the bottom panel of Figure 13, the correlation coefficient would increase to 0.92. This may be because the NCAR aircraft was south of the NOAA aircraft on leg 5, so its ground track was closer to that of leg 8.

Because legs 5 and 8 were traversed in the opposite directions, the time interval was larger at the west end, where the speed of translation (Figure 4) was lower, and smaller at the east end, where the speed of translation was higher. The result was an almost constant relative shift of about 3.5 km along the ground track for the transects shown in the bottom panel of Figure 13.

Since the data on legs 5 and 8 were not collected simultaneously, the standard deviation of the positional errors on each leg would be expected to be about 50 m, and the relative positional error between legs 5 and 8 would be expected to be about 70 m. This estimate is quite reasonable for the measurements we have presented here (see appendix for more discussion), and it is a negligible uncertainty compared with the observed 3.5-km displacement of the SST pattern between those two transects. Even though a larger relative error is possible, it seems highly improbable that it would be exactly aligned with the 60° internal wave propagation direction.

Since leg 5 was at 60° and leg 8 was offset about 400 m south,

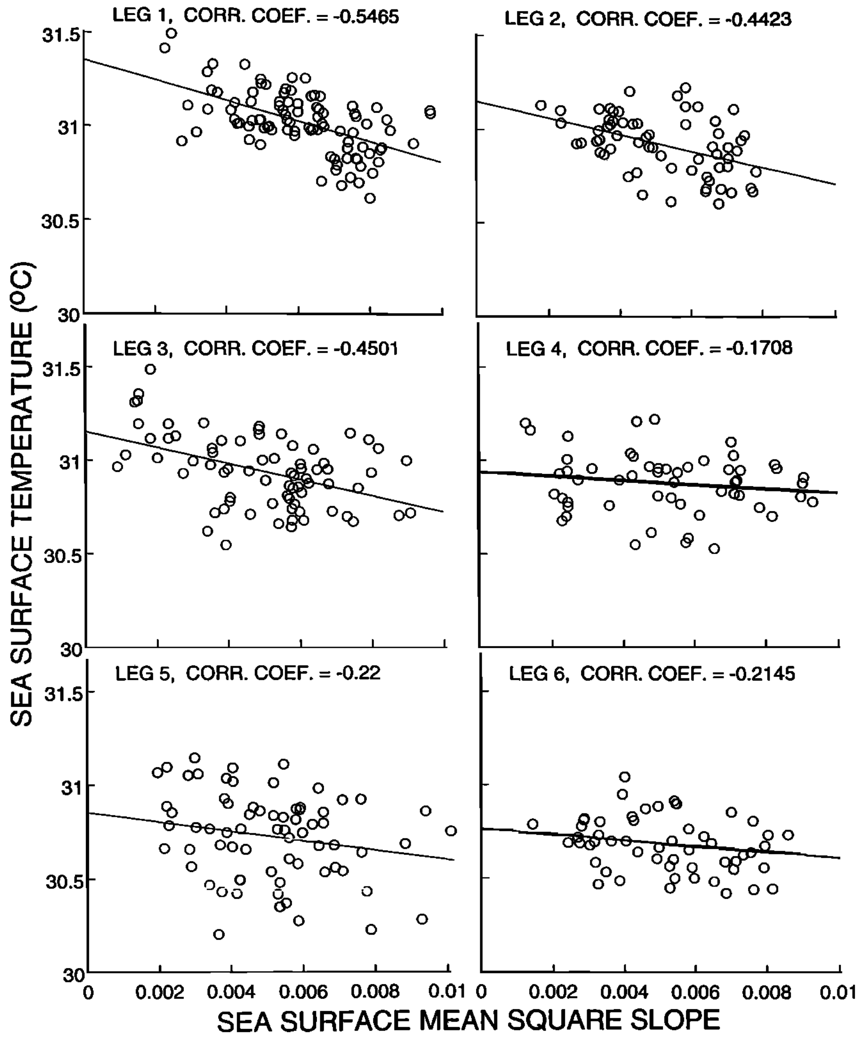

Figure 10. SST data points for each of flight lines 1–6 versus mss with linear regression lines.

aligning the longitude values in Figure 13 actually shifts the relative positions 200 m too far. The end of the southwest transit (leg 8) occurred 4440 s after the start of the northeast transit (leg 5), so aligning the longitudes would overstate the required current by 4.5 cm s^{-1} at the west end of leg 5. Similarly, the start of leg 8 occurred 2870 s after the end of leg 5, so the current required for alignment would be overstated by 7 cm s^{-1} at the east end of leg 5. This would reduce the multiplicative factor on the current from the 1.68 used in Figure 4 to about 1.58, still well above the observed current.

6. Internal Wave Modulation of Diurnal Surface Layer

In this section we will look for evidence that the diurnal surface layer was modulated by internal waves. In that context it is useful to contrast the diurnal surface layer temporal variation at the IMET buoy on November 28, 1992, with that for another light wind day reported by *Soloviev and Lukas* [1997]. The top panel of Figure 14 shows temperature profiles made by Soloviev and Lukas on May 3, 1994, within 25 km of 0°N, 148.2°E, at 1302 (dotted), 1501 (solid), and 1700 (dashed) local solar times (LST).

During calm, sunny afternoons in the western equatorial Pacific, the gradient in the diurnal surface layer can be as large as 4°C m^{-1} [*Ravier-Hay and Godfrey*, 1993; *Fairall et al.*, 1996a; *Soloviev and Lukas*, 1997], and the dotted curve in the top panel of Figure 14 is an example. At 1302 LST the wind speed averaged only 0.5 m s^{-1} and the highest temperature gradient occurred closest to the surface. At 1501 LST the wind was 2.3 m s^{-1} and a shallow mixed layer had been generated right at the surface. The temperature increase in the layer was higher and the depth more shallow than predicted by the TOGA COARE bulk algorithm, so the wind had probably only recently increased to that level and the layer was still in transition. At 1700 LST, the wind averaged 3.7 m s^{-1} and the diurnal surface layer had deepened and its peak temperature had decreased significantly.

The bottom panel of Figure 14 shows the IMET temperature profiles on November 28 at 0240, 0440, and 0640 UTC, which are within 4 min of the same three local solar times as the *Soloviev and Lukas* [1997] profiles. The abscissa for the IMET profiles has been shifted by 0.5°C relative to the Soloviev and Lukas data, since the mixed layer was cooler by about that amount. The wind speed relative to the surface measured at 3.54-m height at IMET averaged 1.6 m s^{-1} from 0000 UTC through 0500 UTC, which included the first two profiles. This agrees with the aircraft wind speed measurements, which averaged 1.6 m s^{-1} over the experiment region and showed negligible temporal trend. The wind decreased to about 1 m s^{-1} by the third profile, which was after the aircraft data considered here were acquired. The IMET temperature profiles showed much less temporal trend over the 4-hour period than the Soloviev and Lukas data did because the wind showed little trend. This makes it easier to observe transients caused by internal waves.

Figure 15a shows the temporal variation of the net shortwave radiation at both IMET and R/V *Moana Wave*, and the total heat flux measured by IMET. Figure 15b shows the *Moana Wave* sea temperature (ST) at 5-cm depth and the IMET measurement closest to the surface from a TPOD at 45-cm depth. Also shown are the temperature at 2-m depth from a SEACAT at IMET (solid line) and the TOGA COARE bulk algorithm prediction of the peak diurnal surface layer temperature (dashed line).

The top meter of the sea absorbs about half of the incoming

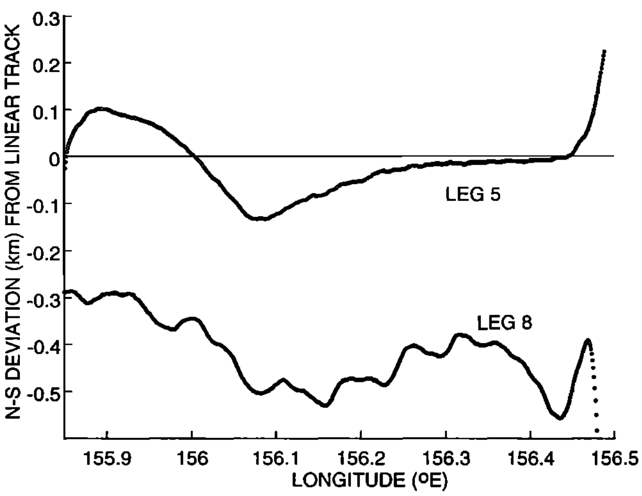

Figure 12. North-south deviation of legs 5 and 8 from a straight line.

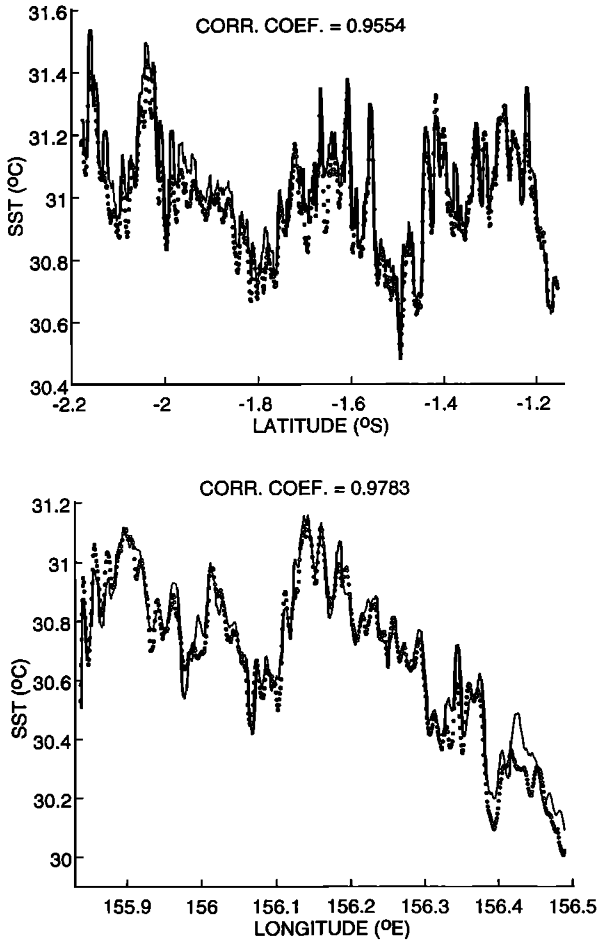

Figure 11. SST data on (top) leg 1 and (bottom) leg 5 from the PRT-5 radiometer (solid curve) on the NOAA WP-3D aircraft N43RF, and the simultaneously collected JPL radiometer (dots) on the NCAR Electra aircraft 308D which was flying wingtip-to-wingtip with the NOAA aircraft. These 1-s data points have been smoothed with a 9-point boxcar filter. The fuselage of the Electra was about 100 m to the right of the P-3 on both legs. For leg 1 comparison only, the Electra data were shifted by 1 s because it encountered the SST features earlier than the P-3. For the leg 5 comparison only, a constant bias of 0.2°C was added to the JPL data points.

solar radiation, and the warming response is similar in the 5- and 45-cm-depth temperature increases. Under the light wind conditions the diurnal surface layer remained shallow, and there was little temperature increase observed initially at 2-m depth. However, as the insolation decreased, the effect of wind-driven mixing became more apparent, and the near-surface temperature of the diurnal surface layer began to decrease.

There is a period in the afternoon when the net heat flux is still positive but the layer is cooling and deepening. Shortly after 0500 on November 28, the layer at the IMET mooring deepened to approximately 2.0 m for an hour, then restratified, and finally deepened past 2.0 m again as the net heat flux became negative. At night, radiative cooling drives ocean convection and a decrease in SST. The layer deepens, cooling the surface and warming the water below. By 1300, approaching local midnight, the warmed water had been mixed down, and the temperature differed very little between 0.45 and 5 m depth. Our interest in particular, however, is in the period in the afternoon when transient deepening occurred at IMET. During this time the sensitivity of the shallow diurnal mixed layer to external processes that modify the depth of the layer should be great.

Figure 15c shows the wind speed relative to the surface at both *Moana Wave* and IMET. Figure 15d shows 26°, 27°, and 28°C isotherms generated from IMET SEACAT data, which had 4 times the temporal resolution of the TPOD data used to generate the isotherms of Figure 3. In addition to the dominant semidiurnal period, there are excursions with about 20-m amplitude and a 3- to 4-hour period, and 7- to 8-m excursions with half hour periods.

Figure 16 shows TPOD temperature profiles for an 8-hour interval which includes the aircraft data acquisition period. In the first 2 hours (0310–0510) there was little variation apparent in these data taken at 15-min intervals. In the next hour (0510–0610) the diurnal surface layer deepened significantly. In the next half hour (0610–0640) it moved back up, almost to its starting position. Then it started moving back down again. After 0700, vertical oscillations are still apparent, but the total heat flux is negative (Figure 15a), and the diurnal surface layer is cooling and deepening progressively.

The TPOD measurements used to develop the profiles of

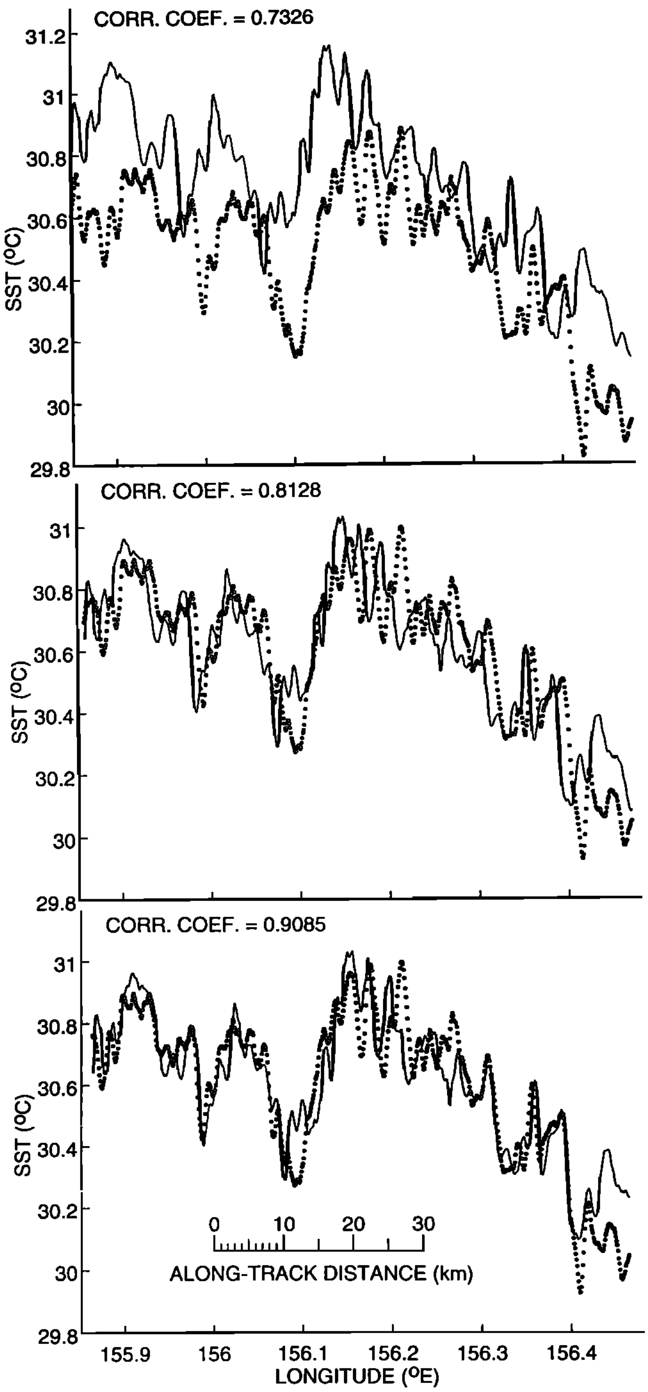

Figure 13. (top) N43RF PRT-5 data from leg 5 (northeast transect) (solid curve, repeated from the bottom panel of Figure 11) and from leg 8 (southwest transect) about 1 hour later (dots). (Middle) Same two curves, but advected by the current to a common reference time halfway between the two transects and corrected for the measured sea surface cooling rate of 0.24°C h^{-1}. (bottom) Same curves, but with the current assumed to be larger than the observed current by a factor of 1.68. The kilometer scale indicates the along-track distance for the ground track oriented at 60°.

Figure 16 were made only at 15-min intervals, and they showed little variability between 0310 and 0455. To obtain higher temporal resolution, the TPOD profiles were used to relate the temperature at 2-m depth to the depth of the 30°C isotherm. Those results for the first 31 profiles of Figure 16 are shown in Figure 17 (profile 32 did not reach 30°C). The equation of the line in Figure 17 is

$$d_{30} = 2 + 1.1(t_2 - 30), \qquad (1)$$

where d_{30} is the depth in meters of the 30°C isotherm, and t_2 is the temperature in degrees Celsius at 2-m depth.

The solid circles in Figure 17, in order of increasing depth, correspond to the following profiles in Figure 16: 1, 2, 6, 8, 15, 17, 24, 22, 11, and 12. Those profiles are reproduced in Figure 18, with profile 1 dotted, profile 2 dashed, profile 6 solid, profile 8 dotted, etc. The simple linear relationship (1) accounts for both the changing thickness and corresponding change in temperature gradient in the diurnal surface layer. Some of the outliers are caused by apparent anomalies in the temperature profiles (7 and 16, for example), while those below 2.5 m are caused by the lack of observations between that depth and 4.65 m.

Relationship (1) breaks down when the layer becomes mixed. We can apply (1) to the 3.75-min data from the SEACAT at 2-m depth to obtain a higher temporal resolution for the 30°C isotherm than is provided by the TPOD 15-min data interval. The result is presented in Figure 19a. Figure 19b is the 30°C isotherm at 15-min resolution determined from the TPOD profiles of Figure 16. Figure 19c shows the 28°C, 27°C, and 26°C isotherms from the SEACAT data of Figure 15, and Figure 19d shows the 24°C, 21°C, 19°C, and 15°C isotherms from the TPOD data of Figure 3.

The structure apparent in the SEACAT data suggests that the 15-min-resolution TPOD data were aliased. There is general agreement between the isotherms above 25°C, but there are also indications of the complexity of the internal wave field. At the dotted vertical line there is no local displacement of either the 30°C or the 24°C isotherm, whereas the 28°C, 27°C,

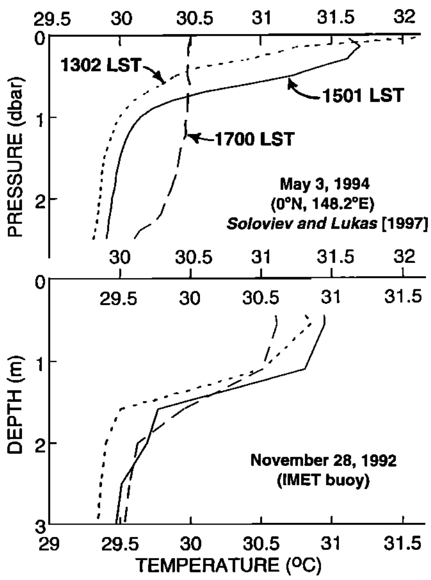

Figure 14. (top) Temperature profiles measured by *Soloviev and Lukas* [1997] on May 3, 1994, in the vicinity of 0°N, 148.2°E, at 1302 (dotted), 1501 (solid), and 1700 (dashed) local solar times (LST), with average wind speeds of 0.5 m s^{-1}, 2.3 m s^{-1} and 3.7 m s^{-1}, respectively. (bottom) IMET temperature profiles on November 28, 1992, for the same three LSTs.

and 26°C isotherms are depressed and the 19°C and 15°C isotherms are elevated, suggesting higher-mode motion.

Figure 20 is a blowup of the SEACAT data from Figure 19, with the addition of the current at 5-m depth. There is strong agreement between the 20-min-period oscillations in the isotherms on the main thermocline and in the diurnal surface layer. The excursions are a significantly higher percentage of the mean isotherm depth in the surface layer (about 15–30%) than they are on the main thermocline (about 5–10%).

7. Internal Wave Modulation of SST

Section 5 indicated that the SST variability can be successfully interpreted as patterns propagating toward 60°. In section 6 we saw that internal waves propagating on the main thermocline can modulate the thickness of the diurnal surface layer and induce currents in it. What is not clear at this point is the exact nature of the physical process that would result in the SST signatures we have observed. We will examine our observations in the context of other experiments to develop a better sense of the attributes a proposed physical mechanism should have.

Jessup and Hesany [1996] found that the downwind side of surface gravity wave crests was warmer than the upwind side whenever the wind was either aligned with or opposed to the swell propagation direction. They suggested that the effect was caused by disruption of the cool skin by small-scale wave breaking. The 1-km averages used in this paper smoothed over any individual surface gravity wave effects, but it seems likely that the SST spatial patterns we observed were more than just a surface manifestation. Were that the case, there should have been a much higher correlation between SST and mss than was observed (Figure 10), and the sign of the correlation would have been positive. If small-scale wave breaking disrupted the cool skin, then the warm areas would have been rougher, not smoother.

That the SST patterns reflect a bulk effect is suggested by the R/V *Moana Wave* 5-cm depth temperature (and, to a lesser extent, the 45-cm depth IMET measurements) showing similar magnitude excursions relative to the TOGA COARE bulk algorithm prediction (Figure 15) as occurred in the aircraft measurements of SST (Figure 13).

Sea surface slicks and roughness variation have long been associated with internal wave propagation in the thermocline [e.g., *LaFond and Cox*, 1962; *Liu et al.*, 1998]. In the classical theory, however, internal waves produce no SST signature. Water initially at the surface never leaves it. Each incremental subsurface temperature layer alternately thins and thickens as the internal wave passes by, so that the temperature gradient varies inversely as the depth of the layer, preserving the SST.

McLeish [1968] studied the IR signature of wind slicks (Langmuir cells). They are aligned in the downwind direction and occur on a much smaller scale than we are concerned with, but his investigation still provides some insight. McLeish found that the patterns were shown more clearly by an IR line scanner than by visible photographs because the temperature signature was stronger than the roughness variation that made the slicks appear as dark lines on the photographs. This is similar to the situation found in Figure 10. Slicks form from the accumulation of surfactants, which damp the capillary waves. The reduction in mss would depend on the surfactant concentrations available in the area. However, the downwelling associated with convergence zones and the upwelling in between would be affecting the water itself. *Langmuir* [1938] indicated that the water in convergence zones had been at the surface longer than the water between them.

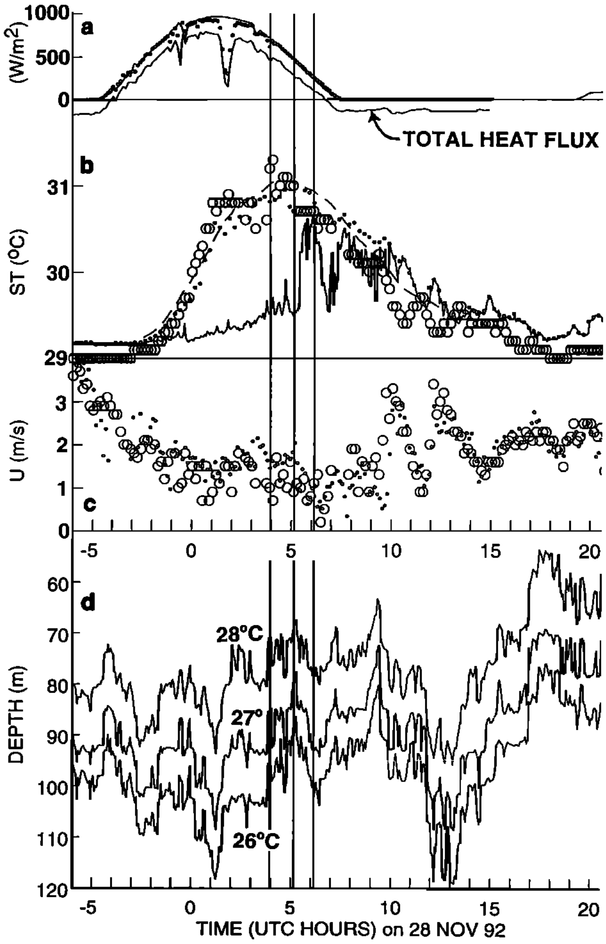

Figure 15. (a) Net shortwave radiation at R/V *Moana Wave* (solid line) and IMET buoy (dots) and total heat flux (solid line). (b) *Moana Wave* sea temperature (ST) at 5-cm depth (circles) and IMET ST at 45-cm depth (dots) and 2-m depth (solid), and prediction of the TOGA COARE bulk algorithm (dashed line). (c) Wind speed relative to the sea surface at *Moana Wave* (circles) and IMET (dots). (d) The 26, 27, and 28°C isotherms. The three vertical lines indicate the starting time of leg 1 (Figure 1), the midpoint time of leg 5, and the midpoint time of leg 8 (nearly a retrace of leg 5 flown in the opposite direction) about 1 hour later.

Fedorov and Ginsburg [1988] (see pp. 140–144 of the English translation) cite several references indicating that internal waves penetrate into the diurnal surface layer and create a system of quasi-horizontal convergent-divergent motions that redistribute the heat accumulated during the day under light wind conditions. None of the measurements cited by *Fedorov and Ginsburg* [1988] included SST. However, near-surface sea temperature measured with a sensor or multiple sensors towed at fixed depths showed fluctuations with amplitudes of 0.5°–1.5°C and horizontal scales of about 1–5 km. During the 34th cruise of the R/V *Akademik Kurchatov*, for example, a sensor towed at 0.15-m depth in the region of the Peruvian coastal upwelling [*Zatsepin et al.*, 1984] demonstrated temperatures 0.3°–0.6°C higher in the slick bands corresponding to areas of convergence located over the rear slopes of internal wave

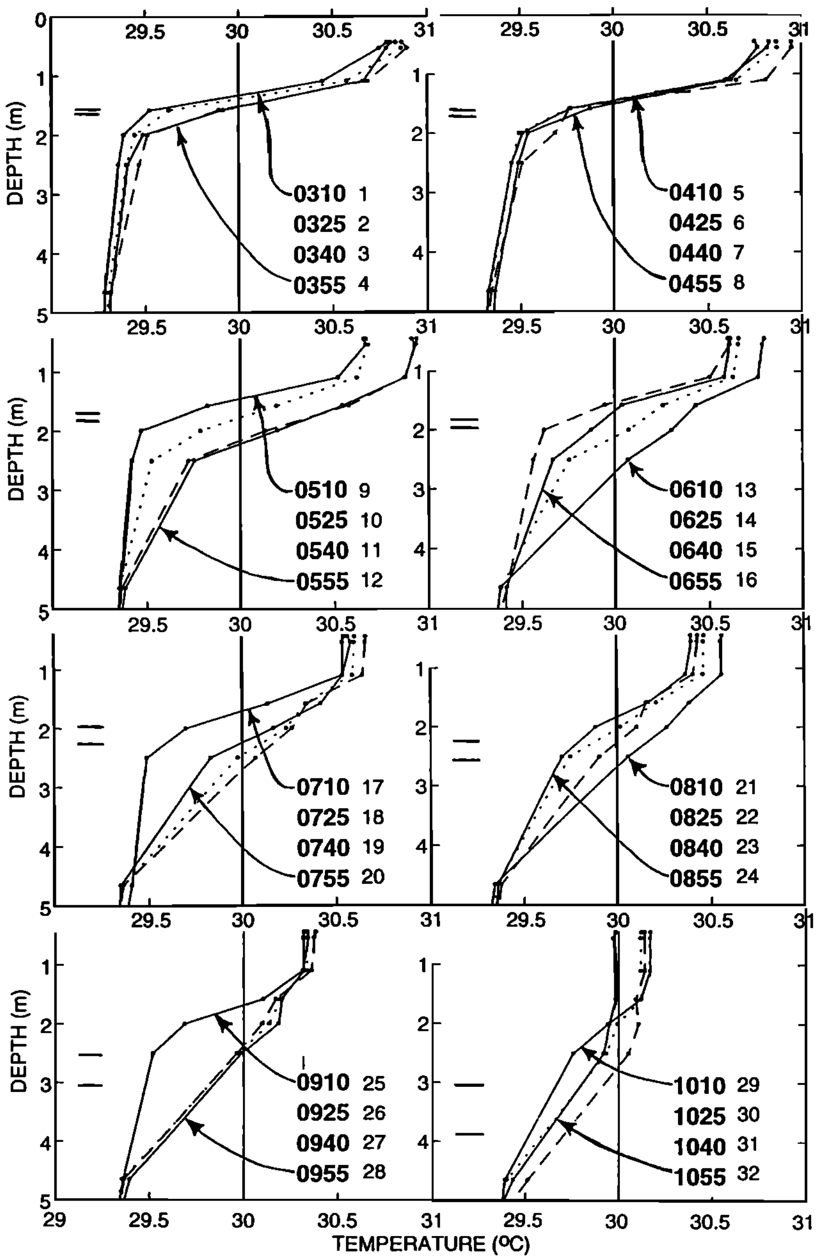

Figure 16. TPOD sea temperature profiles for an 8-hour interval which includes the aircraft data acquisition period. In all panels, the dotted profile is for 25 min past the hour, and the dashed profile is for 40 min past the hour.

crests than in the bands of ripples in between, and on the 27th cruise a sensor at 0.15-m depth in the Sargasso Sea indicated a 0.6°C temperature variation, while another sensor at 3-m depth showed little variation. This is similar to the situation shown in Figure 16. Subsurface temperature variations do not prove that there is a SST signature, but such large variations so close to the surface strongly suggest it.

Implicit in the fixed phase relationship between the internal waves and the shallow depth temperature variations is the presumption that the temperature disturbance propagates with the phase speed of the associated internal waves. This suggests that the internal waves are organizing processes in the diurnal surface layer that affect its near surface temperature. The original Russian references were not reviewed, but *Fedorov and Ginsburg* [1988] offered no suggestion as to how the observed warm water regions could propagate with the phase speed of the internal waves they were associated with.

The wind-driven shear in the layer varies inversely with layer depth. Shoaling would increase shear and thus entrainment at the base, while deepening would reduce the wind-driven flow and perhaps bring shear below the critical level for overturning. If the Richardson number goes above the critical value, mixing is cut off. In Figure 16, the short pairs of horizontal lines at the 29.2°C abscissa position indicate the predicted depth of the diurnal surface layer at the beginning and end of each hour. The predictions, computed from the *Fairall et al.* [1996a], warm layer model show a remarkable accuracy when compared with the highest profile during each hour. This suggests that the diurnal surface layer is in its normal state except when the trough of an internal wave passes by, at which time it

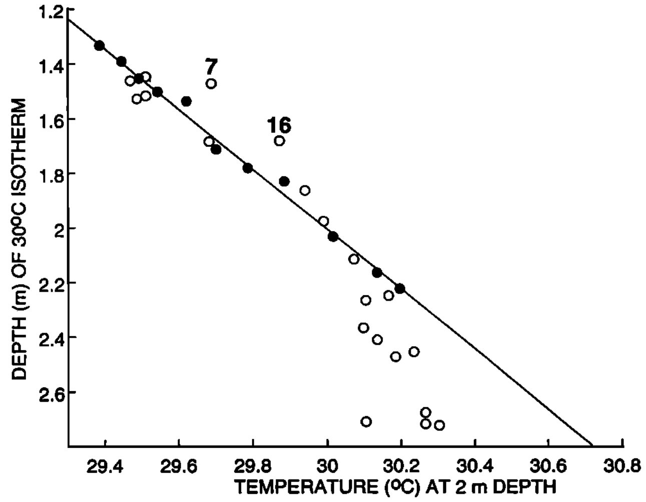

Figure 17. Depth of the 30°C isotherm versus the temperature at 2-m depth, developed from the TPOD profiles of Figure 16. The solid circles in Figure 17, in order of increasing depth, correspond to profiles 1, 2, 6, 8, 15, 17, 24, 22, 11, and 12 of Figure 16.

significantly deepens, disrupting the normal processes within the layer. This image is also supported by the 30°C isotherm in Figure 20.

The dashed curves of Figure 4 suggest that the phase speed of the 2- to 8-km features that aligned so well in the bottom panel of Figure 13 was in the 0.8 to 1.2 m s^{-1} range, a factor of about 1.6 times the current speed. This rate of translation is much slower than the 3 m s^{-1} phase speed of the semidiurnal tide. However, the general situation displayed in Figure 3 is more complex than a single mode 1 internal wave of semidiurnal period. There are significant oscillations with periods less than an hour, and not all the isotherms rise and fall together. For example, the 5 cm s^{-1} current speed excursion at the position indicated by the dotted line corresponds to significant local rises in the 15°C and 19°C isotherms, while the 24°C and 27°C isotherms are descending locally. This suggests the presence of a higher-mode wave.

Figure 21 shows an analysis of the phase speeds versus wavelength for the first five internal wave modes calculated from the N^2 profile obtained by averaging three conductivity-temperature-depth (CTD) profiles taken at R/V *Vickers* (2°S, 156.25°E)

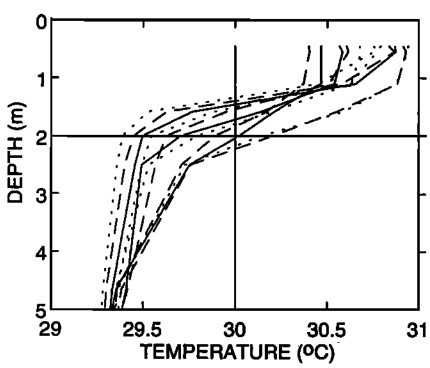

Figure 18. Profiles 1, 2, 6, 8, 15, 17, 24, 22, 11, and 12 reproduced from Figure 16 (corresponding to solid circles in Figure 17, in order of increasing depth), with profile 1 dotted, profile 2 dashed, profile 6 solid, profile 8 dotted, etc.

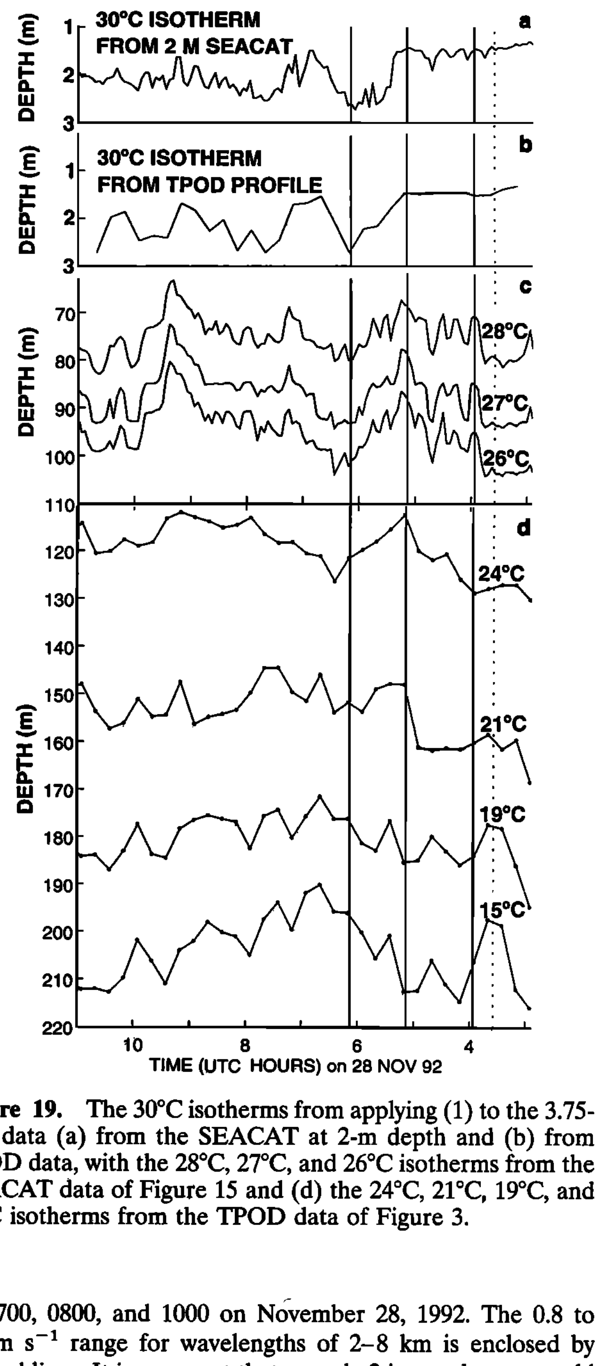

Figure 19. The 30°C isotherms from applying (1) to the 3.75-min data (a) from the SEACAT at 2-m depth and (b) from TPOD data, with the 28°C, 27°C, and 26°C isotherms from the SEACAT data of Figure 15 and (d) the 24°C, 21°C, 19°C, and 15°C isotherms from the TPOD data of Figure 3.

at 0700, 0800, and 1000 on November 28, 1992. The 0.8 to 1.2 m s^{-1} range for wavelengths of 2–8 km is enclosed by dashed lines. It is apparent that a mode 2 internal wave would have the requisite phase speed, and mode 2 is consistent with some of the out-of-phase isotherm height variations seen in the data.

The phase speed calculation for Figure 21 did not include the current, but its effect was probably small. The current shown in Figure 3 was approximately constant within the mixed layer. However, below ~40 or 50 m depth, its speed diminished rapidly, becoming less than 10 cm s^{-1} by the bottom of the thermocline, and during that process the current direction spiraled in a clockwise fashion.

If the phase speeds are to match, the 2- to 8-km-wavelength SST features observed from the aircraft would have to be caused by 2- to 8-km-wavelength mode 2 internal waves propagating toward 60°, the same direction as the internal tide. It might just be considered coincidence that the short-wavelength internal waves propagated in the same direction as the internal

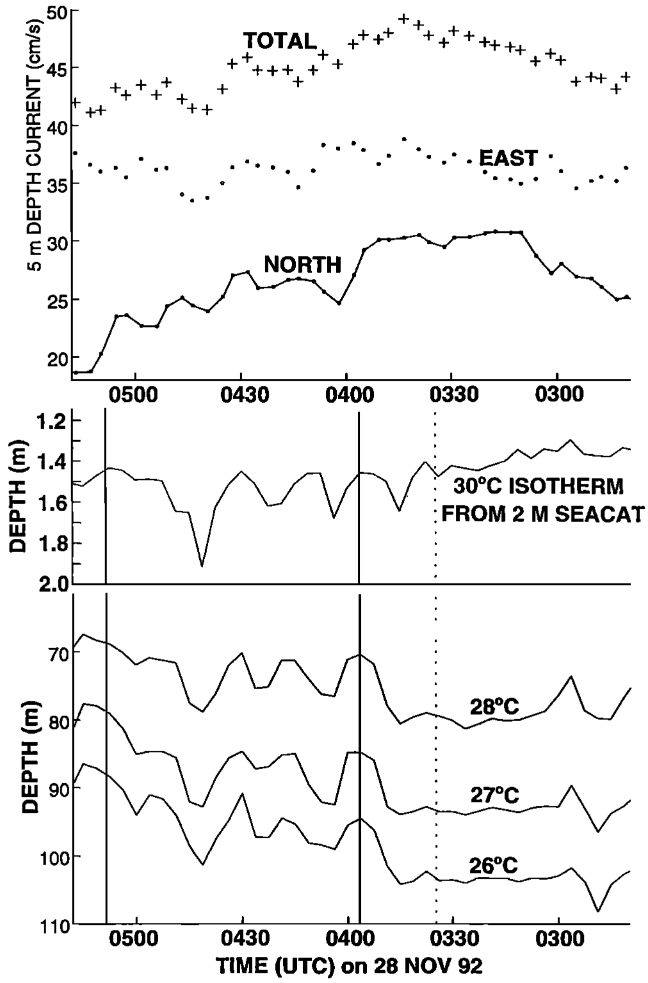

Figure 20. (top) The IMET current at 5-m depth and (bottom) blowups of the SEACAT data from Figure 19.

tide or they may have been of parasitic origin, but it seems implausible that their propagation direction could be significantly different from 60° and still maintain the coherence demonstrated in the bottom panel of Figure 13. If these 2- to 8-km features were actually propagating in some significantly different direction, the apparent phase speed along the 60° flight direction would be correspondingly higher. The 60° propagation direction is also suggested by the wingtip-to-wingtip data (Figure 11), which indicated that the SST features were elongated in the direction perpendicular to 60°.

8. Discussion and Conclusions

The observation of an SST signal propagating relative to the underlying water is unusual. We have presented evidence of persistent SST spatial patterns whose temperature variations are not well correlated with either wind speed or the mean square slope of the sea surface. The SST patterns examined here propagated at a speed (0.8–1.2 m s^{-1}) that was too fast to be caused by the current (0.4–0.7 m s^{-1}), and too slow to be explained by the wind speed (2 m s^{-1}) or the wind speed relative to the surface (1.6 m s^{-1}). We have shown that internal waves on the main thermocline can modulate the thickness of the diurnal surface layer, principally causing it to deepen with the passage of a trough, disrupting the normal processes within the layer. The SST spatial pattern translation speed is comparable to that of mode 2 internal waves of similar wavelength.

The many sea surface sensors employed in COARE on the afternoon of November 28, 1998, caught the upper ocean in an interesting state. The surface was apparently cooling at a mean rate of 0.24°C h^{-1}, under the influence of an air-sea heat flux which should cause warming. Clearly, entrainment of subsurface water was occurring, even though the local wind speed was only 1.6 m s^{-1}. The extreme strains associated with internal wave modulation of the surface layer redistribute waters that are initially laterally homogeneous, producing subsurface temperature patterns that propagate at wave phase velocities. However, patterns in SST, which also appear to propagate, are seen as well. Some form of mixing must be invoked such that the subsurface patterns penetrate to the sea surface.

Can internal wave modulation of the mean entrainment rate cause the propagating patterns? We note that the vertical excursions of the surface layer are of the order of 1 m only 1 m below the surface. The local wind stress, while weak during this period, is distributed over a layer whose depth is strongly modulated by the internal waves. Spatial variation in the subsurface shear must result. The large near-surface strains should correspond to lateral surface particle displacements that are a significant fraction of the horizontal wavelength of the waves. The internal waves themselves embody lateral motions that extend far below the diurnal surface layer. However, some shear will be imparted across the layer, and this can either reinforce or negate the wind driven shear.

We conjecture that as the afternoon progresses and near-surface stability decreases, internal-wave-related influences begin to modulate the near-surface entrainment rate. SST is, of course, the integrated effect of all previous heating and entrainment. In an initially homogenous ocean with cooling rate modulated by a single internal wave component, mixing will produce temperature patterns that initially grow with time but eventually vanish after the internal wave has moved a complete wavelength. For a more complex, nonrepeating pattern of modulation, a moving surface temperature signature will always be present, although the apparent propagation speed will not always reflect the phase speed of the internal waves.

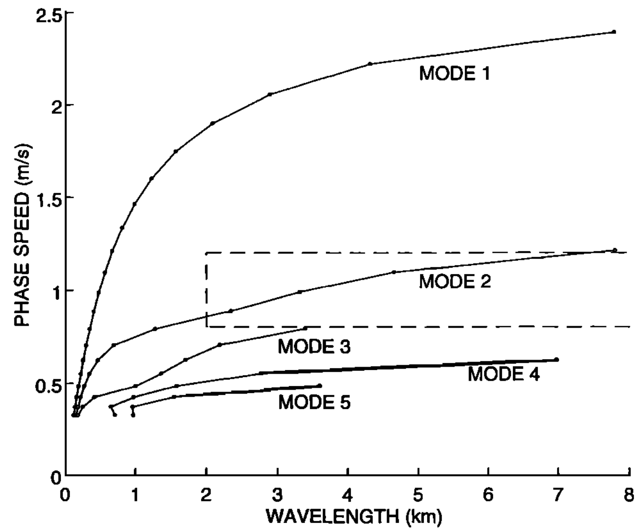

Figure 21. Phase speed versus wave length for the first five internal wave modes calculated from measurements made by R/V *Vickers* (2°S, 156.25°E).

We note that internal wave propagation conditions on November 28 were nearly nondispersive over horizontal wavelengths 4 km and greater (Figure 21). Also, the observed shift in the SST pattern of 3.5 km is comparable to the scale of the smallest features observed, but much smaller than the scale of the most energetic SST signal component. Relative to the wavelengths of the SST pattern, only a modest amount of signal propagation has occurred.

The cooling rate model does not imply that the observed SST patterns correlate perfectly with underlying internal wave displacements. Rather, SST represents the integrated effect of previous cooling. Measurements that can establish the direct relationship between radiometric SST and the subsurface motion field are required to identify the mechanism more precisely.

Appendix

On legs 1 and 5 of Figure 1, NOAA WP-3D aircraft N43RF flew wingtip to wingtip with NCAR Electra aircraft 308D at 60-m height with about 100-m separation between their fuselages. There was also a third aircraft, NOAA WP-3D N42RF, in front of them on these two legs to form a tight triangle. All three aircraft carried GPS receivers. There are intentional errors systematically introduced into the GPS Selected Availability (SA) orbits and clocks to reduce the real-time absolute accuracy of the system to about 50 m. But for aircraft flying in formation, the absolute errors would be identical and their relative positions would be good to 2 to 5 m (W. B. Krabill, NASA GSFC, personal communication, 1997).

The GPS-corrected Inertial Navigation Equipment (INE) position data for the NOAA aircraft indicated that N43RF was 80 m behind and 60 m to the left of N42RF on leg 1, and 60 m behind and 50 m to the left of it on leg 5. The relative positions varied over a range of ~50 m along-track and 20–30 m laterally. These mean positions and relative variations are consistent with the images of N43RF recorded by a side-looking video camera on NCAR Electra 308D during these two legs.

NASA Goddard Space Flight Center has had an Arctic Ice Mapping (AIM) program in operation since 1991 to monitor the elevation of the Greenland ice sheet [*Krabill et al.*, 1995]. They map the elevations over a swath with a conical scanning laser from an aircraft flying 400 m above the terrain. The ground track is controlled by a guidance system that uses a single GPS receiver and the SA signal [*Wright and Swift*, 1996] to fly great circle ground tracks defined by preset way points. The exact GPS orbits are obtained several weeks post-flight and combined in a differential technique with the aircraft GPS receiver data and simultaneously acquired ground receiver data to produce aircraft trajectories whose absolute accuracy is 10 cm. This allows an assessment of the real-time accuracy of the aircraft guidance system.

The project guidelines were that the swaths from one year to another must have at least a 50% overlap everywhere to ensure that the height difference could be assessed. A wide swath requires the laser to have a large off-nadir incidence angle, which degrades the measurements due to uncertainties in aircraft roll attitude. Initially, used a 15° incidence angle was used to achieve a 200-m swath. Because the ground tracks were found to be so accurate in earlier missions, in 1994 the incidence angle was reduced to 10° (140-m swath width). The 70-m relative positional standard deviation (half swath overlap) for two transects flown at different times demonstrated in the AIM program is the same relative standard deviation we have assumed in our assessment of the SST pattern translation speed.

In 1997, ten flight lines of 100- to 300-km length flown in earlier years were repeated. The earlier ground tracks were found to be so accurate, even with oscillations attributable to the aircraft–guidance system interaction, that none of the way points needed to be moved for the repeat mission (R. N. Swift, personal communication, 1998).

Acknowledgments. The authors acknowledge the invaluable contributions of all the scientists, engineers, technicians and flight crews, who made TOGA COARE possible. E.J.W. thanks Peggy LeMone of NCAR for discussions and access to the data from the forward- and side-looking video cameras on the NCAR Electra, and Alexander Soloviev for discussions on his observations. He also thanks E. F. Bradley of the CSIRO, and Earl Gossard, Lev Ostrovsky, Andre Smirnov, Len Fedor, and many other colleagues at NOAA ETL for numerous discussions. D. E. Hines maintains the SRA, and he, D. W. Shirk, and G. S. McIntire installed the system in the NOAA WP-3D aircraft for the TOGA COARE deployment. G. S. McIntire and J. L. Ward were in the Solomon Islands with the SRA. The authors thank A. Plueddemann and M. Tomczak for the use of TPOD, Seacat, and ADCP data from the IMET mooring, and A. Plueddemann, S. Anderson, and the WHOI Upper Ocean Processes Group for help with the mooring deployment, recovery, and subsequent data processing. R.P. thanks the officers and crew of the R/V *Vickers*. He was supported by National Science Foundation grant ATM-9110553. E.J.W. and D.E.H. were supported by the NASA Office of Earth Science. D.E.H. was also supported by the NOAA Climate Division. D.P.R. was supported by NOAA and the Office of Naval Research. The work of S.P.B. was supported by NSF grants ATM-9024436 and ATM-9110540 and NOAA 56GP0154-01. R.A.W. was supported by the National Science Foundation, grant ATM95-25844.

References

Apel, J. R., J. R. Holbrook, A. K. Liu, and J. J. Tsai, The Sulu Sea internal soliton experiment, *J. Phys. Oceanogr.*, *15*, 1625–1651, 1985.

Etkin, V. S., A. V. Kuzmin, and Yu. G. Trokhimovsky, IR and microwave sea surface observations under calm weather conditions, in *IGARSS'92, International Space Year: Space Remote Sensing, 92CH3041-1*, pp. 260–262, IEEE, Piscataway, N. J., 1992.

Ewing, G. C., Relation between band slicks at the surface and internal waves in the sea, *Science*, *3*, 91–94, 1950.

Fairall, C. W., E. F. Bradley, J. S. Godfrey, G. A. Wick, J. B. Edson, and G. S. Young, Cool skin and warm-layer effects on sea surface temperature, *J. Geophys. Res.*, *101*, 1295–1308, 1996a.

Fairall, C. W., E. F. Bradley, D. P. Rogers, J. B. Edson, and G. S. Young, Bulk parameterization of air-sea fluxes for Tropical Ocean–Global Atmosphere Coupled Ocean-Atmosphere Response Experiment, *J. Geophys. Res.*, *101*, 3747–3764, 1996b.

Fedorov, K. N., and A. I. Ginsburg, *Pripoverkhnostnyi sloi okeana*, 303 pp., Gidrometeoizdat, Moscow, 1988. (English translation, *The Near-Surface Layer of the Ocean*, translated by M. Rosenberg, 259 pp., VSP, Zeist, Netherlands, 1992.)

Garrett, C., and W. Munk, Internal waves in the ocean, *Annu. Rev. Fluid Mech.*, *11*, 339–369, 1979.

Hagan, D. E., The profile of upwelling 11-μm radiance through the atmospheric boundary layer overlying the ocean, *J. Geophys. Res.*, *93*, 5294–5302, 1988.

Hagan, D. E., D. P. Rogers, C. A. Friehe, R. A. Weller, and E. J. Walsh, Aircraft observations of sea surface temperature variability in the tropical Pacific, *J. Geophys. Res.*, *102*, 15,733–15,747, 1997.

Jessup, A. T., and V. Hesany, Modulation of ocean skin temperature by swell waves, *J. Geophys. Res.*, *101*, 6501–6511, 1996.

Krabill, W. B., R. H. Thomas, C. F. Martin, R. N. Swift, and E. B. Frederick, Accuracy of airborne laser altimetry over the Greenland ice sheet, *Int. J. Remote Sens.*, *16*, 1211–1222, 1995.

Kropfli, R. A., L. A. Ostrovsky, T. Stanton, E. A. Skirta, A. N. Keane, and V. Irisov, Relationships between strong internal waves in the coastal zone and their radar and radiometric signatures, *J. Geophys. Res.*, in press, 1998.

LaFond, E. C., and C. S. Cox, Internal waves, in *The Sea*, vol. 1, edited by M. N. Hill, pp. 731–763, Interscience, New York, 1962.

Langmuir, I., Surface motion of water induced by wind, *Science*, *87*, 119–123, 1938.

Liu, A. K., Y. S. Chang, M. K. Hsu, and N. K. Liang, Evolution of nonlinear internal waves in the East and South China Seas, *J. Geophys. Res.*, *103*, 7995–8008, 1998.

McLeish, W., On the mechanisms of wind-slick generation, *Deep Sea Res.*, *15*, 461–469, 1968.

Pinkel, R., M. Merrifield, J. Picaut, L. Washburn, S. Rutledge, M. McPhaden, and D. Siegal, Solitary internal waves in the western equatorial Pacific Ocean, *Geophys. Res. Lett.*, *24*, 1603–1606, 1997.

Price, J. F., R. A. Weller, and R. Pinkel, Diurnal cycling: observations and models of the upper ocean response to diurnal heating, cooling and wind mixing, *J. Geophys. Res.*, *91*, 8411–8427, 1986.

Ravier-Hay, P., and J. S. Godfrey, A model of diurnal changes in sea surface temperature for the western equatorial Pacific, *TOGA Notes 11*, pp. 5–8, Nova Southeast. Univ., Dania, Fla., 1993.

Saunders, P. M., Aerial measurement of sea surface temperature in the infrared, *J. Geophys. Res.*, *72*, 4109–4117, 1967.

Serra, Y. L., D. P. Rogers, D. E. Hagan, C. A. Friehe, R. L. Grossman, R. A. Weller, and S. Anderson, The atmospheric boundary layer over the central and western equatorial Pacific Ocean observed during COARE and CEPEX, *J. Geophys. Res.*, *102*, 23,217–23,237, 1997.

Soloviev, A., and R. Lukas, Observation of large diurnal warming events in the near-surface layer of the western equatorial Pacific warm pool, *Deep Sea Res.*, *Part I*, *44*, 1055–1076, 1997.

Walsh, E. J., et al., Observations of sea surface mean square slope under light wind during the Tropical Ocean–Global Atmosphere Coupled Ocean-Atmosphere Response Experiment, *J. Geophys. Res.*, this issue.

Webster, P. J., and R. Lukas, TOGA COARE: The Tropical Ocean–Global Atmosphere Coupled Ocean-Atmosphere Response Experiment, *Bull. Am. Meteorol. Soc.*, *73*, 1377–1416, 1992.

Weller, R., and S. Anderson, Surface meteorology and air-sea fluxes in a western equatorial Pacific warm pool during the TOGA Coupled Ocean-Atmosphere Response Experiment, *J. Clim.*, *9*, 1959–1990, 1996.

Wright, C. W., and R. N. Swift, Application of new GPS aircraft control/display system to topography mapping of the Greenland ice cap, in *Proceedings of the Second International Airborne Remote Sensing Conference and Exhibition: Technology, Measurement, and Analysis*, pp. I-591–I-599, Environ. Res. Inst. of Mich., Ann Arbor, 1996.

Zatsepin, A. G., A. S. Kazmin, and K. N. Fedorov, Thermal and visible manifestations of large internal waves on the ocean surface (in Russian), *Okeanologiya*, *24*, 586–592, 1984. (English translation, *Oceanology*, Engl. Transl., *24*(4), 444–449, 1984.)

M. Baumgartner and R. A. Weller, Woods Hole Oceanographic Institution, Woods Hole, MA 02543.

S. P. Burns, Department of Mechanical Engineering, University of California, Irvine, CA 92717.

C. W. Fairall and E. J. Walsh (corresponding author), NOAA Environmental Technology Laboratory, R/E/ET6, 325 Broadway, Boulder, CO 80303-3328. (e-mail: ewalsh@etl.noaa.gov)

D. E. Hagan, Jet Propulsion Laboratory, California Institute of Technology, 4800 Oak Grove Drive, Pasadena, CA 91109-8099.

R. Pinkel and D. P. Rogers, Scripps Institution of Oceanography, University of California, San Diego, La Jolla, CA 92093.

(Received May 29, 1997; revised March 10, 1998;
accepted March 13, 1998.)